SPi | Journal Code: J G R B | Article ID 53317 | Dispatch: 20.02.19 | CE: RFS | No. of Pages: 17 | ME:

Revised proofs are sent only in the case of extensive corrections upon request.

AGU100 ADVANCING EARTH AND SPACE SCIENCE

JGR Solid Earth

RESEARCH ARTICLE
10.1029/2018JB016903

Key Points:
- Creep rates of polycrystalline magnetite aggregates were measured as a function of temperature, stress, grain size, and water content
- The presence of water resulted in significantly enhanced magnetite diffusion creep rates
- Flow laws based on the experimental results predict magnetite to be weaker than many silicate minerals under both dry and wet conditions

Correspondence to:
J. L. Till,
jtill@hi.is, jesstill@gmail.com

Citation:
Till, J. L., Rybacki, E., Morales, L. F. G., & Nauman, M. (2019). High-temperature deformation behavior of synthetic polycrystalline magnetite. *Journal of Geophysical Research: Solid Earth*, *124*. https://doi.org/10.1029/2018JB016903

Received 18 OCT 2018
Accepted 8 FEB 2019
Accepted article online 14 FEB 2019

High-Temperature Deformation Behavior of Synthetic Polycrystalline Magnetite

J. L. Till[1,2], E. Rybacki[1], L.F.G. Morales[1,3], and M. Naumann[1]

[1]Deutsches GeoForschungsZentrum Helmholz Zentrum Potsdam, Telegrafenberg, Potsdam, Germany, [2]Institute of Earth Sciences, University of Iceland, Reykjavík, Iceland, [3]Scientific Center for Optical and Electron Microscopy (ScopeM), ETH Zürich, Zürich, Switzerland

Abstract We performed a series of deformation experiments on synthetic magnetite aggregates to characterize the high-temperature rheological behavior of this mineral under nominally dry and hydrous conditions. Grain growth laws for magnetite were additionally determined from a series of static annealing tests. Synthetic magnetite aggregates were formed by hot isostatic pressing of fine-grained magnetite powder at 1,100 °C temperature and 300-MPa confining pressure for 20 hr, resulting in polycrystalline material with a mean grain size around 40 μm and containing 2–4% porosity. Samples were subsequently deformed to axial strains of up to 10% under constant load conditions at temperatures between 900 and 1,150 °C in a triaxial deformation apparatus under 300-MPa confining pressure at applied stresses in the range of 8–385 MPa or in a uniaxial creep rig at atmospheric pressure with stresses of 1–15 MPa. The aggregates exhibit typical power-law creep behavior with a mean stress exponent of 3 at high stresses, indicating a dislocation creep mechanism and a transition to near-Newtonian creep with a mean stress exponent of 1.1 at lower stresses. The presence of water in the magnetite samples resulted in significantly enhanced static grain growth and strain rates. Best-fit flow laws to the data indicate activation energies of around 460 and 310 kJ/mol for dislocation and diffusion creep of nominally dry magnetite, respectively. Based on the experimentally determined flow laws, magnetite is predicted to be weaker than most major silicate phases in relatively dry rocks such as oceanic gabbros during high-temperature crustal deformation.

1. Introduction

Experimental deformation studies are essential for interpreting tectonic and metamorphic histories of rocks from mineral textures and microstructures. Although Fe-Ti oxides are an important class of common crustal minerals, few studies have investigated the high-temperature strength and deformation textures of Fe-Ti-oxide minerals in detail, with the exception of hematite (Siemes et al., 2008, 2003, 2011). Magnetite occurs widely as an accessory mineral in igneous rocks and is abundant in iron ore deposits and banded iron formations. Additionally, core samples from oceanic core complexes recovered during several ocean drilling expeditions have been found to contain intervals of oxide gabbros rich in ilmenite and magnetite. These oxide-rich rocks are frequently associated with high-temperature ductile shear zones and strain localization in oceanic gabbros from slow- and ultraslow-spreading ridges (Blackman et al., 2006; Karson et al., 1997; Natland, 2002), leading to speculations that the oxides are rheologically weak phases that facilitate low-temperature ductility (Agar & Lloyd, 1997).

A small number of earlier studies have reported experimental magnetite deformation results for single crystals and polycrystalline samples over a limited range of temperature and stress (Crouch & Robertson, 1990; Domınguez-Rodrıguez et al., 2002; Hennig-Michaeli & Siemes, 1975, 1982; Muller & Siemes, 1972). However, no previously proposed flow laws have been based on robust experimental data. In addition, better understanding of the high-temperature strength of magnetite can improve interpretations of magnetic anisotropy in terms of bulk petrofabrics in deformed magnetite-bearing rocks (Till & Moskowitz, 2014) and may even facilitate semiquantitative strain determinations through magnetic methods (Till et al., 2012).

The deformation behavior of magnetite and related ferrite minerals can also serve as an analog for less studied spinel-structured phases such as chromite, Mg-Al-spinel, and ringwoodite, which are difficult to investigate experimentally. As a deep mantle phase, ringwoodite is particularly challenging to study in

Table 1
Conditions for Magnetite Grain Growth Experiments and Porosity Estimates From Image Analysis of Hot Isostatic Pressed Samples

Experiment	Temp (°C)	Time (hr)	d (μm)	Porosity (%)
MGG01	1,000	20	22 ± 2	1.6
MGG02	1,050	20	27 ± 1	1.7
MGG03	1,150	20	60 ± 1	1.7
MGG04	950	20	19 ± 2	2.9
MGG05	1,100	6	27 ± 1	1.2
MGG06	1,100	44	50 ± 1	2.9
MGG07	1,100	3	19 ± 1	2.6
MGG08	1,100	20	39 ± 1	1.9
MGH01[a]	1,100	20	66 ± 5	5.8

[a]Hydrous sample.

laboratory settings, so some experimental efforts have focused instead on the properties of spinel-structured germanates in order to predict the deformation behavior of ringwoodite (Dupas-Bruzek et al., 1998; Lawlis et al., 2001; Vaughan & Kohlstedt, 1981). Magnetite is an ideal model for such isostructural spinel phases due to the ready availability of high purity material, stability under suitably oxidizing laboratory conditions, and a convenient range of strength and deformation temperatures.

Here we report results from the first systematic investigation of the high-temperature rheological behavior of magnetite. We performed a series of laboratory creep experiments on synthetic magnetite aggregates deformed in coaxial compression under ductile conditions. The experimental data were used to derive empirical creep equations for magnetite, which are compared with experimental deformation data for various rock-forming silicate minerals to predict relative strain partitioning with magnetite at geological conditions.

2. Materials and Methods

2.1. Sample Synthesis

The starting material used in all experiments is a commercially produced magnetite powder (Kremer Pigmente GmbH) with an initial mean grain size around 2 μm. To produce dry polycrystalline aggregates for deformation, sample powders were first cold-pressed into open-ended cylindrical Ni capsules with dimensions of 20 mm by 10 mm under a uniaxial pressure of approximately 400 MPa. Capsules were then annealed by hot isostatic pressing (HIP) at a temperature of 1,100 °C under 300-MPa confining pressure, P_c, for 20 hr to promote compaction and grain growth. The mean grain size following these HIP conditions is 39 ± 3 μm based on image analysis of a polished surface using the Image J software (Table 1 and Figure 1a).

To investigate the grain-size dependence of magnetite creep, finer-grained starting material was produced by limiting the HIP durations to 3 or 6 hr at 1,100 °C, which yielded mean grain sizes of 19 and 27 ± 2 μm, respectively (Figure 1b), as determined by electron backscatter diffraction (EBSD) measurements. Another series of HIP tests was performed at various durations and temperatures between 950 and 1,150 °C to characterize the grain-growth kinetics of magnetite (Figure 1d). The cold-pressing procedures for grain-growth experiments were identical to those used for creep experiments except that 10 × 10 mm Ni capsules closed at both ends were used. Conditions for the grain-growth annealing experiments are listed in Table 1, which also lists porosity of these HIPed samples determined from image analysis. Porosity estimates are between 1% and 3% for all samples, with slightly larger values for samples HIPed at lower temperatures. Density determinations using Archimedes' method indicated that the density of magnetite samples after a 20-hr HIP at 1,100 °C exceeded 98% of that of a magnetite single crystal, indicating a porosity of around 2%. The hot-pressed aggregates consist of equant grains with high-angle triple junctions and abundant small pores, which are mainly located at grain boundaries but occasionally occur within grains (Figure 1a). The average sample dimensions after HIPing are approximately 8 mm in diameter by 17 mm in length.

The bulk magnetite composition determined by electron microprobe analysis in weight percent oxides is 91.54% FeO (with total Fe calculated as FeO), 0.03% TiO_2, 0.16% SiO_2, 0.30% MnO, 0.02% CaO, 0.11% Al_2O_3, 0.12% MgO, and 0.02% Ni. The total content of substitutional impurities is therefore less than 0.80 wt%. No additional phases were observed in the HIPed material. Some amount of cation exchange between the Ni jacket and the adjacent magnetite was observed in the HIPed material. The composition of the sample adjacent to the jacket contains 12% NiO, which decreases to 0.2% NiO at a distance of 230 μm from the jacket. The Ni-substituted sample rim is assumed to be a solid solution between Ni-ferrite (trevorite) and magnetite and accounts for about 6% of the total sample volume. Based on the shared structure and similar melting temperatures (1,927 K for trevorite compared with 1,870 K for magnetite), the presence of a local trevorite component at the sample rim is expected to have a negligible influence on the overall strength of the magnetite.

To investigate the effect of water on the creep behavior of magnetite, hydrous samples were synthesized by adding 1.0 wt% of fine-grained lepidocrocite (γ-FeOOH) powder to the magnetite powder, which was

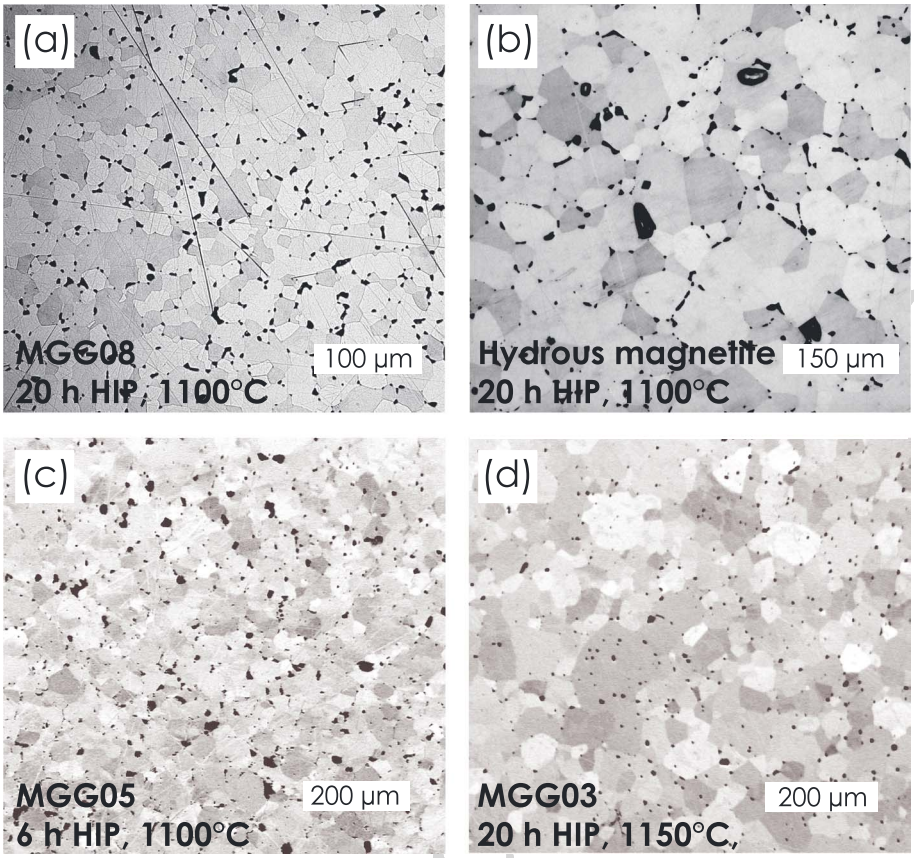

Figure 1. Images of grain structure in magnetite aggregates HIPed at various conditions. (a and b) Reflected light photomicrographs of sample surfaces etched in acid to make grains boundaries more visible. (c and d) Scanning electron microscope images of synthetic magnetite aggregates taken in orientation contrast mode. Dark areas are pore spaces. Note the different scales in each image. HIP = hot isostatic press.

thoroughly mixed before HIPing. Lepidocrocite undergoes dehydroxylation at approximately 250 °C to produce magnetite and water vapor (Till et al., 2014) through the reaction

$$6FeOOH \rightarrow 2Fe_3O_4 + 3H_2O + \frac{1}{2}O_2. \quad (1)$$

The addition of 1 wt% lepidocrocite produces an initial bulk water content of approximately 0.1 wt% in the samples after HIPing. The mean grain size in the hydrous sample MGH01 (Table 1) was significantly larger (66 μm) than in the nominally dry samples for a HIP of 20 hr (Figure 1b), indicating that the additional water content accelerated grain growth. The exact residual water content of the nominally dry samples was not determined, and it is possible that trace amounts of water may remain after HIPing. However, good agreement was found between the creep data from triaxial deformation experiments and uniaxial experiments performed at 0.1 MPa (section 3.2). Since the latter tests ensure dry conditions, this similarity of creep rates suggests that the water fugacity is similarly low in the two sets of samples.

2.2. Creep Experiments

HIP runs and creep experiments were performed in a triaxial Ar gas-medium pressure vessel (Paterson, 1990). The sample assembly for both HIP and creep consists of tapered alumina pistons on either side of the sample capsule and zirconia end pistons, all of which are surrounded by a thin iron jacket (approximately 0.5 mm thick) to isolate the sample assembly from the pressure medium. After HIPing, creep experiments were performed in axial compression under a confining pressure of 300 MPa. Most experiments were conducted at a constant temperature with 7–9 load steps. After deformation, all samples were sectioned vertically through the cylinder center, mounted in epoxy, and polished. The final dimensions of each sample and jacket materials were measured and used to back-calculate the initial sample dimensions

Table 2
Conditions and Results of Magnetite Experiments in the Triaxial Deformation Apparatus

Experiment	Temperature (°C)	Stress (MPa)	Log $\dot{\varepsilon}$ (1/s)	n	cumulative strain (%)	d_f (μm)	Experiment duration (hr)
MP01	1,000	78.0	−5.95	1.3	1.2		
	1,000	29.3	−6.46	1.3	3.2		
	1,000	47.9	−6.18	1.3	3.8		
	1,000	84.6	−5.87	1.3	4.6		
	1,000	103	−5.74	1.3	5.3		
	1,000	130	−5.55	2.3	5.8		
	1,000	157	−5.39	2.3	6.7		
	1,000	194	−5.19	2.3	7.5		
	1,000	229	−4.99	2.3	8.4	44 ± 1	30
MP02	900	190	−6.38	1.6	1.1		
	900	227	−6.23	1.6	1.8		
	900	129	−6.63	1.6	3.0		
	900	252	−6.09	3.6	4.1		
	900	280	−5.94	3.6	4.9		
	900	299	−5.84	3.6	5.5		
	900	339	−5.64	3.6	6.1		
	900	383	−5.40	3.6	6.7	41 ± 1	30
MP03	1,050	41.3	−5.50	1.4	1.8		
	1,050	24.4	−5.81	1.4	2.9		
	1,050	73.9	−5.19	1.4	3.8		
	1,050	89.7	−5.03	1.4	4.8		
	1,050	114	−4.81	2.8	5.7		
	1,050	137	−4.59	2.8	6.7		
	1,050	169	−4.33	2.8	7.9	40 ± 5[a]	4.0
MP04	950	156	−5.93	1.4	1.7		
	950	114	−6.17	1.4	2.7		
	950	52.5	−6.60	1.4	4.2		
	950	191	−5.70	3.2	5.2		
	950	230	−5.50	3.2	6.1		
	950	259	−5.34	3.2	7.2		
	950	288	−5.17	3.2	8.2		
	950	318	−5.01	3.2	9.2	42 ± 3[a]	27
MP05	1,100	32.3	−5.08	1.1	1.2		
	1,100	61.7	−4.77	1.1	3.2		
	1,100	90.6	−4.43	3.1	6.6		
	1,100	114	−4.13	3.1	10.4		
	1,100	136	−3.90	3.1	12.6	46 ± 2	1.0
MP07	1,100	7.26	−5.84	0.9	2.1		
	1,100	24.2	−5.43	0.9	3.5		
	1,100	41.3	−5.18	0.9	4.3		
	1,100	58.4	−4.98	2.2	5.2		
	1,100	75.2	−4.79	2.2	6.0		
	1,100	91.9	−4.60	2.2	6.8		
MP08	1,050	7.5	−5.67	1.1	1.3		

Continuous

Table 2
Continued

Experiment	Temperature (°C)	Stress (MPa)	Log $\dot{\epsilon}$ (1/s)	n	cumulative strain (%)	d_f (μm)	Experiment duration (hr)
	1,050	17.2	−5.45	1.1	1.9		
	1,050	26.3	−5.29	1.1	2.5		
	1,050	45.1	−5.07	1.1	3.1		
	1,050	63.6	−4.94	1.1	3.7		
	1,050	81.9	−4.81	1.1	4.5		
	1,050	119	−4.57	1.1	5.0		
	1,050	157	−4.35	1.1	5.7	19 ± 2[a]	4.2
MP09	1,050	9.1	−5.96	1.1	1.5		
	1,050	18.0	−5.76	1.1	2.5		
	1,050	26.9	−5.63	1.1	3.5		
	1,050	45.1	−5.41	1.1	4.4		
	1,050	63.0	−5.28	1.1	5.1		
	1,050	81.0	−5.15	1.1	5.8		
	1,050	117	−4.89	1.1	6.5		
	1,050	153	−4.64	1.1	7.3	26 ± 2[a]	6.6
MP10[b]	1,100	8.8	−5.03	1.0	0.9		
	1,100	26.5	−4.63	1.0	2.3		
	1,100	35.3	−4.47	1.0	3.1		
	1,100	43.4	−4.33	1.0	4.2		
	1,100	61.2	−4.10	1.0	5.6		
	1,050	8.6	−5.69	1.0	5.2		
	1,050	17.3	−5.49	1.0	6.5		
	1,050	34.9	−5.16	1.0	7.5		
	1,050	61.3	−4.81	1.0	8.2		
	1,050	97.1	−4.41	1.0	8.6		
	1,000	27.3	−5.85	1.1	9.6		
	1,000	54.2	−5.52	1.1	10.0		
	1,000	81.6	−5.24	1.1	10.4	59 ± 5[a]	4.4

[a]Grain size estimates from reflected light image analysis.
[b]Hydrous sample.

at the end of the HIP stage using the measured total piston displacement from each creep run and assuming constant sample volume. Samples do not exhibit any evidence of reaction at the interface between the alumina spacers and magnetite during HIP or deformation.

Sample stresses were corrected for the strength of the jacketing materials using flow laws for Fe and Ni from Frost and Ashby (1982). The flow stresses in each creep segment were calculated from the force measured by the internal load cell and the calculated changes in the cross-sectional areas of both the jacket and sample that supported the load, which increased continuously during shortening. Load steps were limited to increments of 1–2% strain after steady state deformation was achieved. The stress calculations assume a constant volume and uniform sample shortening, which is a reasonable assumption for the limited total strains used in the experiments. Barreling of the cylindrical samples was minimal in most experiments. The stresses and strain rates listed in Table 2 were taken from the final portion of each load step. Temperature uncertainties are <0.5%, and the reported stress and strain rate data are accurate to within <3% (Rybacki & Dresen, 2000; Rybacki et al., 2006). At the end of each experiment, the actuator movement was stopped so that the piston position remained constant during cooling of the sample to encourage preservation of the dislocation structure.

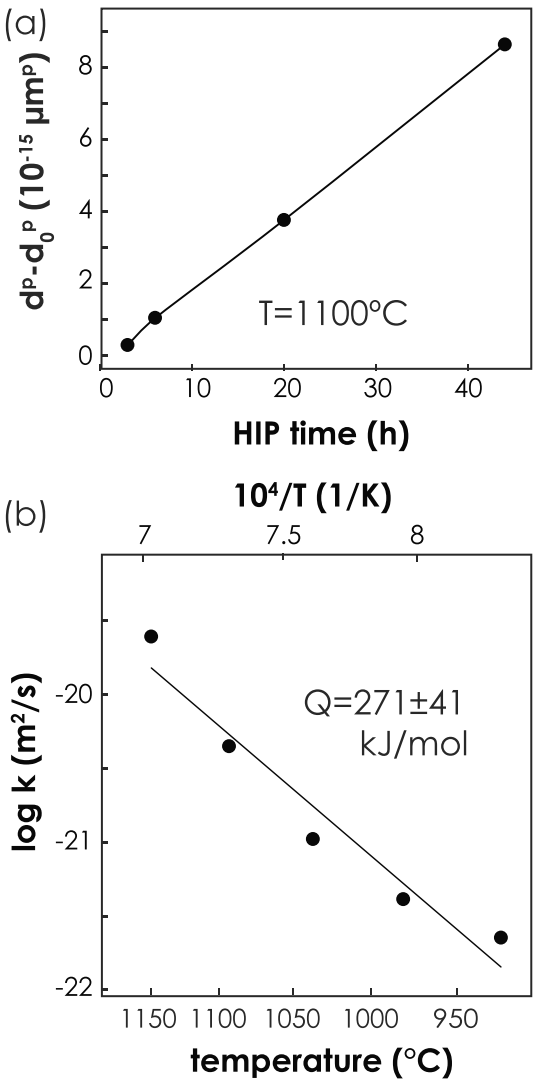

Figure 2. Results of grain growth annealing experiments for magnetite. (a) Results of time series experiments conducted at 1,100 °C demonstrating a nearly linear relationship with time for a grain growth exponent of 3.3. (b) Arrhenius plot indicating temperature dependence of the grain growth constant for magnetite at 20 hr of annealing. HIP = hot isostatic press.

In addition to triaxial experiments performed in the gas-medium apparatus, two uniaxial creep experiments were conducted on polycrystalline magnetite samples at atmospheric pressure (0.1 MPa) in a dead-load rig (Dimanov & Jaoul, 1998; Freund et al., 2004) to achieve low stresses and strain rates with high precision and to estimate the activation volume of creep. Samples for these experiments were HIPed at 1,100 °C for 20 hr and then milled into small cylinders of 2-mm diameter and 4-mm length. The atmosphere in the creep rig consisted of CO_2 gas mixed with 3% H_2, which buffers the oxygen fugacity close to the Ni-NiO buffer (Prunier & Hewitt, 1981) within the magnetite stability field. Recent work by Faul et al. (2018) indicates that oxygen fugacities in the interior of samples buffered by solid metal capsules may differ from that imposed by the capsule at the sample rims. We did not observe any features to suggest that this was the case in our samples; however, the issue should be considered in future studies. Sample MC01 was deformed at multiple load steps at low stresses and five temperatures to determine stress exponents at various temperatures in the diffusion creep regime. A second sample, MC02, was deformed with a constant load at decreasing temperature steps to better characterize the activation energy of diffusion creep.

2.3. Microstructural Analysis

All deformed samples were initially characterized by either reflected light microscopy or in a scanning electron microscope using the forescatter detector to identify orientation contrast in the aggregates. Selected samples were characterized using transmission electron microscopy (TEM) to image dislocation structures in deformed magnetite. TEM foils were prepared via focused ion beam techniques and imaged on a Tecnai G2 F20 X-Twin TEM. EBSD was performed on selected deformed samples and all grain growth annealing experiments to determine grain sizes and crystallographic-preferred orientations (CPO). The EBSD measurements were acquired on an FEI Quanta 3-D FEG focused ion beam/scanning electron microscope with an EDAX-OIM EBSD system. Grain sizes in the samples were determined from EBSD maps containing >5,000 grains using a constant step size of 1 μm during measurements. For samples that were not analyzed by EBSD, grain sizes were determined from grain boundary maps traced from reflected light optical micrographs of sample surfaces that were etched in hydrochloric acid. Image analysis was performed using the grain boundary intercept method with a scaling factor of 1.5 (Hansen et al., 2011). This method slightly underestimates the grain size due to the finite width of the grain boundaries created during etching and tracing.

3. Results

3.1. Grain Growth Kinetics

The grain growth kinetic constant, k, was calculated using the relation $kt = d^p - d_0^p$ commonly used for normal grain growth (Karato, 1989), where t is the annealing time in seconds, p is the grain growth exponent, d is the final grain size in micrometers, and d_0 is the initial grain size of the magnetite powder, estimated to be about 2 μm. For the 3–44-hr time series of grain growth tests conducted at 1,100 °C (Table 1), least squares fitting of the data yields $p = 3.3 \pm 0.2$ (Figure 2a). Whereas grain growth in isotropic, pure, single-phase material is characterized by a value of p around 2 (Atkinson, 1988; Covey-Crump, 1997), the higher value observed here suggests that magnetite grain growth kinetics are affected by the initial porosity or other trace impurities present in the samples (Brook, 1976; Covey-Crump, 1997; Freund et al., 2001). Using a grain growth exponent of 3.3, the values of k were determined for each annealing temperature between 950 and 1,150 °C and plotted on an Arrhenius plot in the form $k = k_0 exp(-Q/RT)$, which yielded an activation energy of $Q = 271 \pm 41$ kJ/mol (Figure 2b).

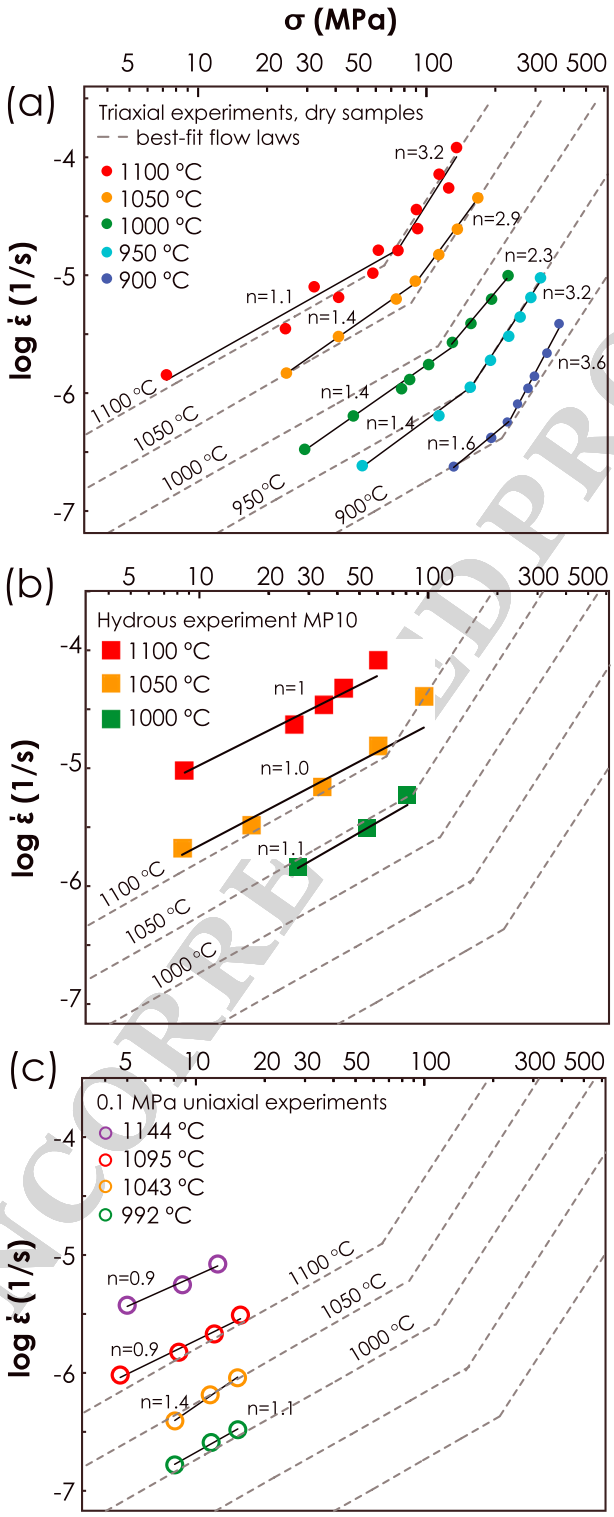

Figure 3. Plots of log (strain rate) versus log (stress) for magnetite aggregates deformed at various temperatures and P_c = 300 MPa. (a) Triaxial deformation results under nominally dry conditions. (b) Triaxial deformation results for hydrous sample MP10. (c) Uniaxial deformation results for sample MC01 deformed at P_c = 0.1 MPa. The dashed lines indicate best-fit flow laws determined from a multilinear regression fit to the data set for dry samples.

Table 3
Conditions and Results of Uniaxial Deformation Experiments on Magnetite Aggregates at 0.1 MPa

Experiment	Temperature (°C)	σ (MPa)	Log $\dot{\epsilon}$ (1/s)	n	% cumulative strain
MC01	1,144	1.1	−5.83	0.9	0.6
	1,144	5.0	−5.43	0.9	1.5
	1,144	8.7	−5.25	0.9	2.2
	1,144	12.4	−5.08	0.9	2.8
	1,095	4.6	−6.02	0.9	3.3
	1,095	8.4	−5.82	0.9	3.8
	1,095	12.0	−5.67	0.9	4.4
	1,095	15.7	−5.51	0.9	5.1
	992	8.1	−6.78	1.1	6.5
	992	11.6	−6.59	1.1	6.6
	992	15.2	−6.48	1.1	6.8
	1,043	8.1	−6.41	1.3	6.9
	1,043	11.5	−6.19	1.3	7.1
	1,043	15.2	−6.04	1.3	7.3
MC02	1,144	8.39	−5.22	n/a	0.9
	1,115	8.26	−5.58	n/a	1.5
	1,074	8.12	−5.91	n/a	1.9
	1,043	7.98	−6.21	n/a	2.5
	1,011	7.88	−6.55	n/a	2.9
	969	7.85	−6.95	n/a	3.5
	937	7.69	−7.24	n/a	3.8

Note. n/a = not applicable.

The grain growth laws were used to assess the need to correct the triaxial creep data for syndeformation grain growth. For samples HIPed at 1,100 °C for 20 hr prior to creep, the maximum increase in grain size predicted was 2 μm based on the creep durations given in Table 2. The measured final grain sizes for these samples ranged between 38 and 46 μm (Table 2), in good agreement with the predicted sizes. Some of this difference is likely due to variations in porosity and initial grain size after HIP between samples. The extent of grain growth during these triaxial experiments was therefore considered to be negligible, and no correction was applied. The finer-grained samples MP08 and MP09 were estimated to grow from 19 to 22 μm and 27 to 29 μm in mean grain diameter, respectively. Because these increases are too small to resolve with image analysis (uncertainty of 2–5 μm), the calculated final grain sizes were used for determining the grain size exponent.

3.2. Creep Experiments

Table 2 displays the results from the series of anhydrous load-stepping experiments performed in the triaxial apparatus along with the hydrous experiment MP10, which included load-stepping segments at multiple temperatures. Steady-state differential stresses for individual creep segments ranged between 7 and 383 MPa with axial strain rates between 2.3×10^{-7} and 1.5×10^{-4} s^{-1}. The first load step of each experiment was typically excluded from the analysis due to settling behavior of the deformation assembly. The total amount of axial shortening was typically less than 10% (Table 2) with most run durations lasting between 3 and 30 hr. The mechanical data for all magnetite aggregates can be described by a power creep law of the form $\dot{\epsilon} = A\sigma^n d^{-m} exp\{-(Q + PV)/RT\}$, where $\dot{\epsilon}$ is strain rate in per second, A is a material-dependent pre-exponential factor, σ is the axial differential stress in megapascal, n is the stress exponent, d is the grain size in micrometers, m is the grain size exponent, Q is the activation energy in joules per molar, P is confining pressure in megapascal, and V is the activation volume in cubic centimeter per molar.

Figure 3a contains a log-log plot of stress versus strain rate for nominally dry samples with an initial grain size of 39 μm in which a transition in stress sensitivity from low to high stresses can be seen for each experiment. F3

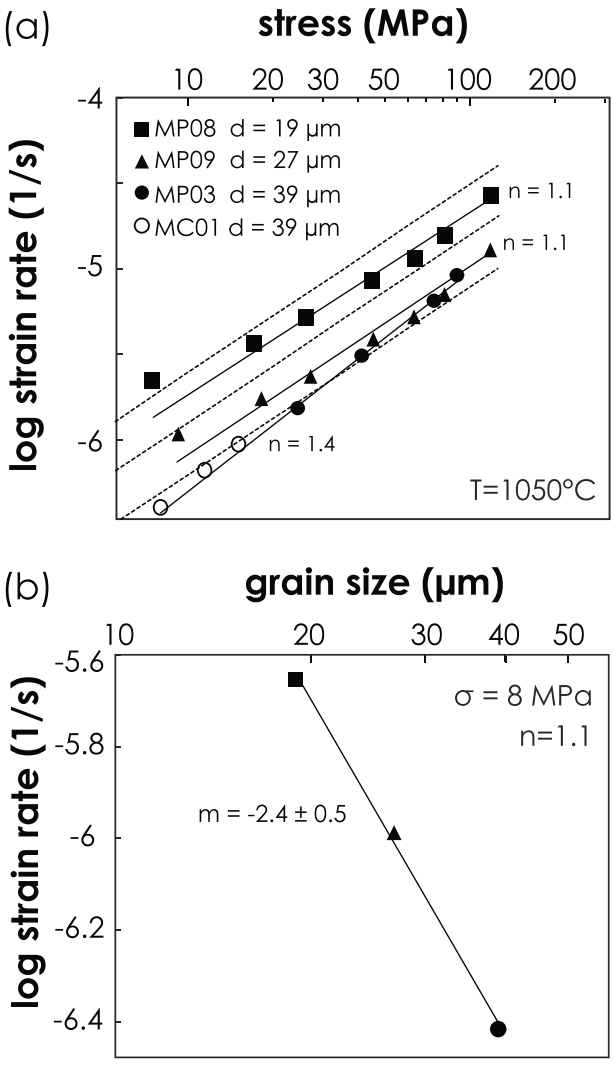

Figure 4. (a) Log strain rate versus stress plot for polycrystalline magnetite samples with different initial grain sizes deformed at 1,050 °C. (b) Log strain rate plotted as a function of grain size for polycrystalline magnetite samples deformed at 1,050 °C normalized to 8 MPa. Dashed lines in (a) are best-fit flow laws, while solid lines are regression fits to individual data sets.

Stress exponents in the low-stress regime range between 1.1 and 1.6 (Figure 3a), with higher values occurring at lower temperatures. These values are slightly higher than the nominal value of 1 for diffusion creep, indicating that the strains rates are dominantly controlled by diffusional processes with a small contribution from a parallel mechanism, such as dislocation creep or dislocation-accommodated grain boundary sliding. Stress exponents in the high-stress regime range from 2.3 to 3.6 with an average of $n = 3.0 \pm 0.5$, which is consistent with a dislocation creep mechanism (Frost & Ashby, 1982).

A single triaxial experiment was performed on hydrous magnetite (sample MP10) immediately following a 22-hr HIP at 1,100 °C with creep temperatures of 1,100, 1,050, and 1,000 °C and 3–5 load-stepping creep segments at each temperature. The water-bearing magnetite sample was significantly weaker than the nominally dry samples deformed at the same temperatures with strain rates that were a factor of 4–6 higher for the wet sample compared to dry samples (Figure 3b). The creep segments in the experiment on the hydrous sample were restricted to relatively low stresses, and stress exponents at each temperature are close to 1. The final grain size of sample MP10 was measured to be $59 \pm 5\mu$m, slightly smaller than the 66 ± 5 μm size of the hydrous HIPed sample MGH01 (Table 1) although the grain sizes overlap within uncertainties.

The results of uniaxial creep experiments are shown in Table 3. Sample MC01, which was deformed at lower axial stresses than the triaxial experiments ($\sigma < 20$ MPa), displayed a mean stress exponent of 1.1 ± 0.2 (Figure 4c) for various temperatures, consistent with diffusion-controlled creep. The uniaxial data are in excellent agreement with the diffusion creep-dominated portion of the triaxial experiments extrapolated to slightly lower stresses.

Triaxial creep data for the finer-grained samples (MP08 and MP09) deformed at low stress also exhibit an average stress exponent of 1.1 (Figure 4a), although there is a slight upward curvature in the data. The creep data from these experiments, together with data from sample MP03, were compared as shown in Figure 4 to determine the approximate grain-size sensitivity of creep in magnetite. For comparison, we normalized the strain rate data to a stress of 8 MPa, assuming a stress exponent of $n = 1.1$ for all experiments. Least squares fitting of the data yields a grain size exponent of $m = -2.4 \pm 0.5$ (Figure 4b). This value lies between the nominal values of $m = -3$ and -2 for grain-boundary diffusion (Coble) creep and volume diffusion (Nabarro-Herring) creep (Nabarro, 1967), respectively. The relatively large uncertainty results from the small number of different grain sizes used.

A best-fit flow law for dislocation creep was determined through a multilinear regression fit to the high-stress data measured in triaxial experiments, while the diffusion creep flow law was similarly determined using the uniaxial experiment data combined with the low-stress data from triaxial experiments. The latter also included an estimate of the effect of different confining pressures (0.1 and 300 MPa) on the resulting creep rates. For the diffusion creep flow law, the grain size exponent was fixed at −2.4. We slightly adjusted the pre-exponential factor to best fit the data lying solely in the diffusion creep regime, excluding data that fall in the transition between diffusion and dislocation creep. The regression results yielded flow law parameters for dislocation creep of $\log A = 7.3 \pm 0.4$ MPa^{-n} s^{-1}, $n = 3 \pm 0.3$, and $Q = 463 \pm 19$ kJ/mol. The best-fit diffusion creep flow law parameters are $\log A = 8.9 \pm 0.6$ MPa^{-n} μm^m s^{-1}, $n = 1.1 \pm 0.1$, $m = -2.4 \pm 0.5$, $Q = 314 \pm 15$ kJ/mol, and $V = 26 \pm 6$ cm^3/mol. Note that the evaluation of V is based on only two confining pressures (0.1 and 300 MPa).

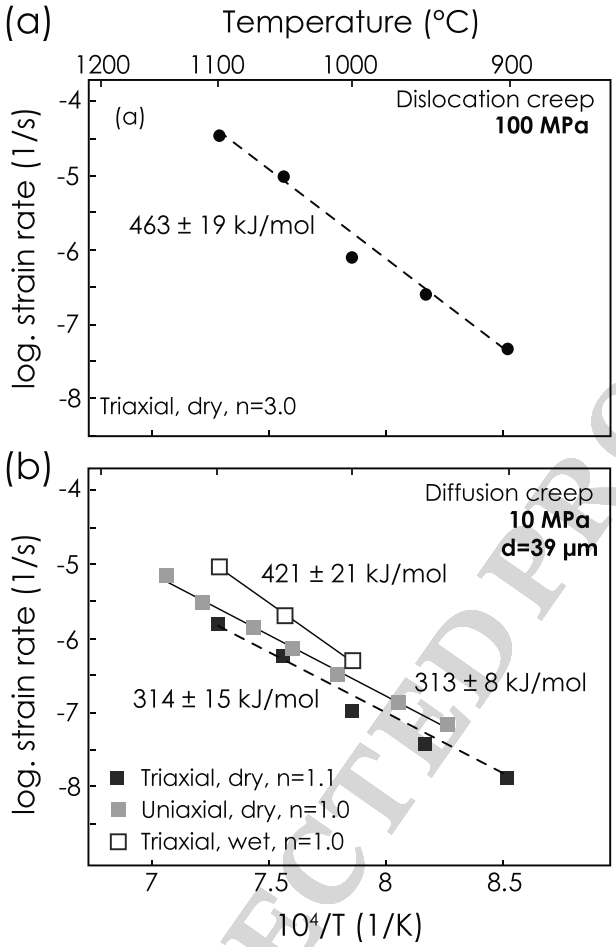

Figure 5. Temperature dependence of magnetite creep rates for the (a) dislocation creep and (b) diffusion creep regimes indicating activation energies for different deformation mechanisms. Creep data are normalized to a constant stress of 100 or 10 MPa for the two regimes. Dashed lines indicate the Arrhenius relations of the best-fit flow laws for each regime, while solid lines in (b) are fits for individual experiments.

Regression lines for the nominally dry data are shown as dashed lines in Figures 3 and 4a for comparison to experimental data. The Arrhenius relations represented by these flow laws are shown with the experimental data normalized to constant stress of 100 MPa for dislocation creep and 10 MPa for diffusion creep in Figure 5. For comparison, the activation energy for diffusion creep determined from the temperature stepping uniaxial creep experiment MC02 (Table 3) is 313 ± 8 kJ/mol, which agrees very well with the multilinear regression result of 314 ± 15 kJ/mol. The normalized creep data from the hydrous experiment MP10 indicates an approximate activation energy of 421 ± 21 kJ/mol in the diffusion creep regime, which is distinctly higher than under dry conditions. F5

3.3. Deformation Microstructures

The estimated porosities in the deformed magnetite aggregates based on image analysis were around 1.5–2.5% for samples deformed in the triaxial apparatus and around 3.1–4.8% for samples deformed in the uniaxial apparatus, which are comparable to the HIPed samples. Because the magnetite grains and grain boundaries cannot be easily seen in reflected light microscopy, EBSD maps were made on several deformed samples to investigate the grain-scale microstructure and presence of CPO. EBSD maps (Figure 6a) contain dominantly equant to slightly elongated grains. EBSD data for deformed samples was also used to produce maps of misorientation within grains (Figure 6b). A significant portion of deformed magnetite grains contain cumulative misorientations of at least 5° across individual grains as a result of dislocation activity. F6

Grain boundaries in the deformed magnetite samples appear less planar and generally exhibit more curvature than those in the hot-pressed magnetite, in particular at low temperature (Figures 1 and 6).

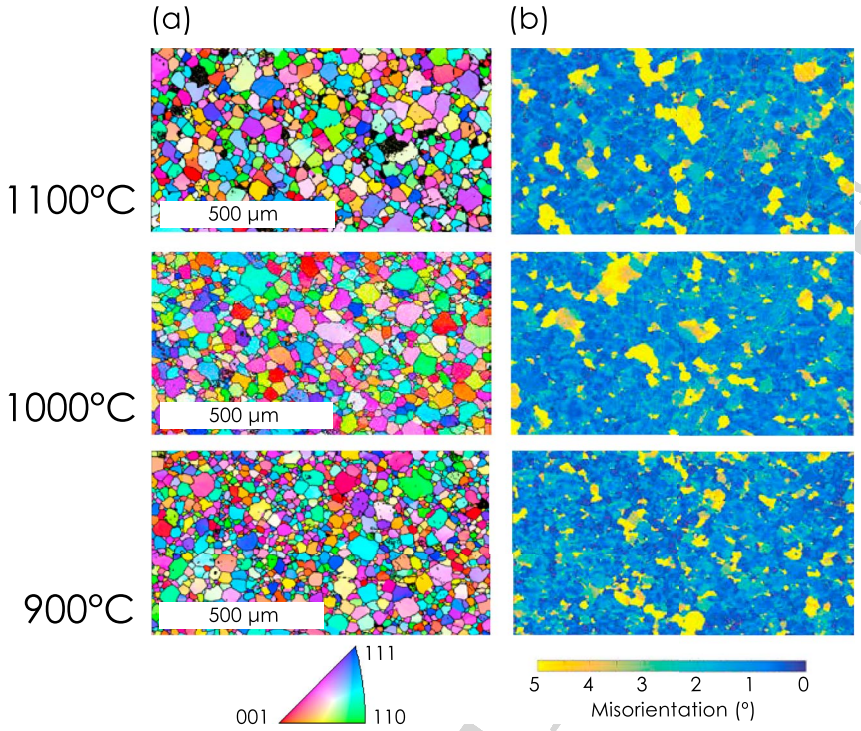

Figure 6. Electron backscatter diffraction maps illustrating the grain microstructures in magnetite samples deformed at T = 1,100, 1,000, and 900 °C (samples MP05, MP01, and MP02). Colors in (a) represent the grain orientations based on the color scheme given by the inverse pole figure at bottom left. Maps in (b) indicate the cumulative intragrain misorientation in individual grains ranging from 0° to 5°. The compression axis is along the vertical direction in the images.

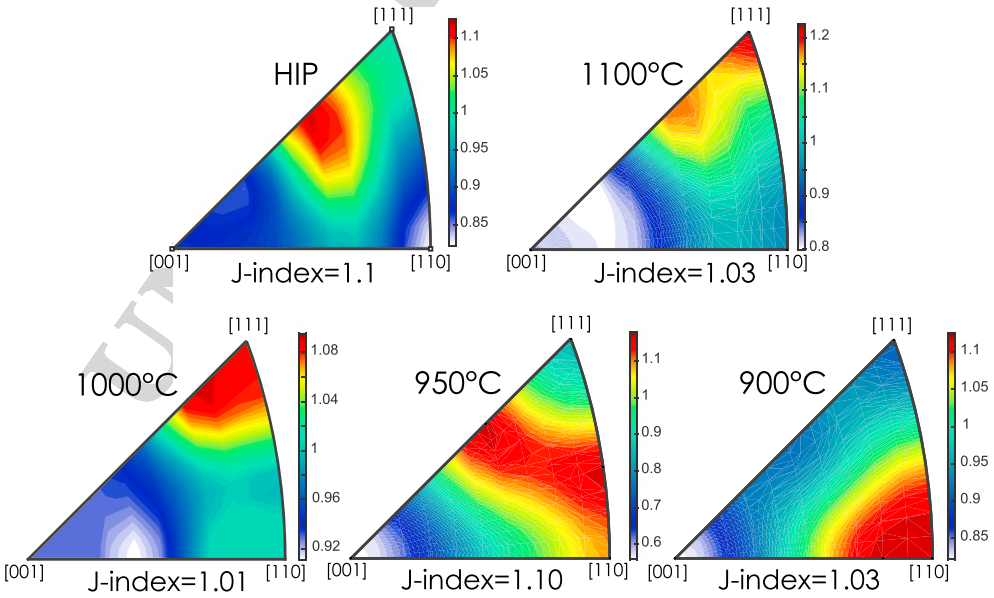

Figure 7. Inverse pole figures of crystallographic orientations in HIPed and deformed magnetite samples. J-index values indicate relative crystallographic-preferred orientation strength. HIP = hot isostatic press.

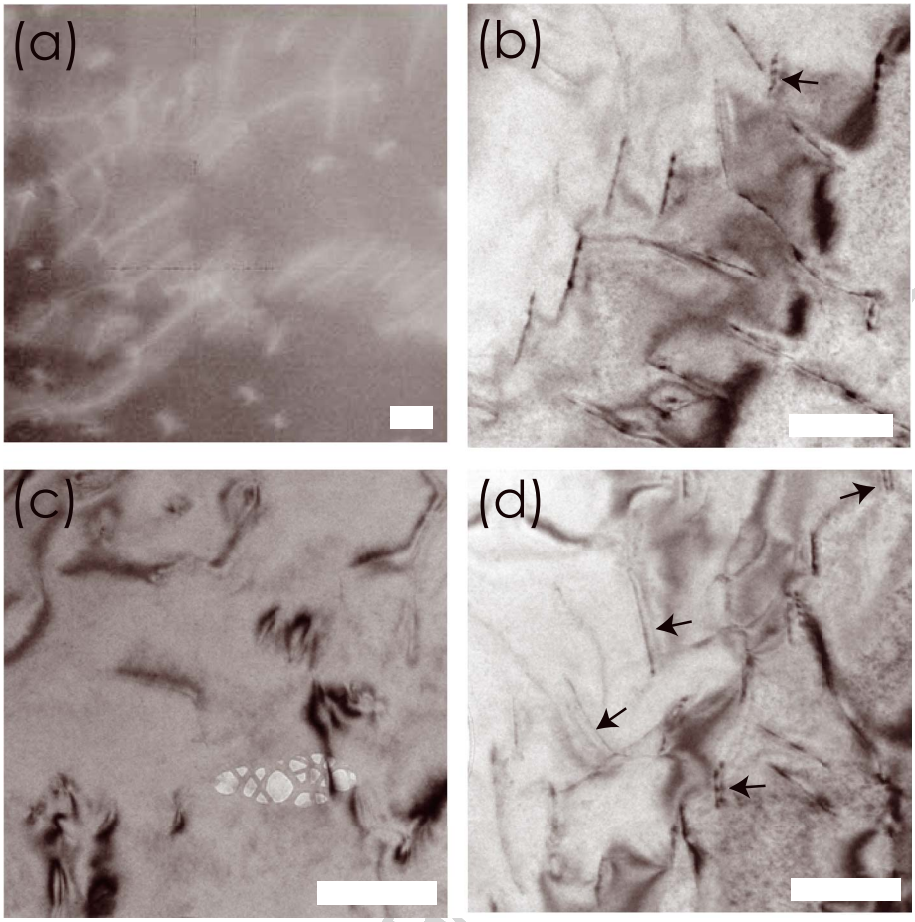

Figure 8. Transmission electron microscopy images of dislocation structures in magnetite deformed at (a) 1,100 °C and (b–d) 950 °C. All images were taken in bright-field mode except (a), which is a dark-field image. Arrows in (b) and (d) indicate dissociated dislocations separated by stacking fault ribbons. Scale bars in each image represent 500 nm.

Crystallographic textures determined by EBSD were visualized for magnetite using inverse pole figures (Figure 7). The degree of CPO indicated by the J-index (Bunge, 1982) is weak and similar between deformed samples and HIPed samples, with maximum values around 1.1. The pole figure maxima are weakly associated with certain crystallographic axes in magnetite for some samples. However, there is no consistent orientation of the crystallographic fabric among experiments at different temperatures considering that the maximum contour densities in inverse pole figures are all lower than 1.2. The low J-index values and low contour densities both indicate that CPO is very weak or absent in the deformed aggregates. Because the total axial strains in the experiments were limited to about 10% and because samples were deformed over a range of stresses, the sample strains within the dislocation creep regime may be too small to allow for significant CPO development during the experiments. The grain sizes of coarse-grained samples are quite similar before and after deformation (Tables 1 and 2), suggesting that no significant grain size reduction or dynamic recrystallization has occurred during dislocation creep of the samples.

Figure 8 contains examples of TEM images of dislocations in samples MP05 and MP04, deformed at 1,100 and 950 °C, respectively. In MP05 (Figure 8a), a mixture of free dislocations and small dislocation tangles was observed that mainly consist of straight or slightly curved segments. MP04 contains predominantly straight dislocations, which often occur in sets of parallel dislocation lines (arrows, Figure 8d). These likely represent dissociated partial dislocations separated by stacking faults, as such dissociation occurs easily in the spinel lattice structure (Hornstra, 1960; Veyssiére & Carter, 1988). In both samples, dislocations are often arranged in loosely clustered linear arrays that may represent precursors to low-angle subgrain boundaries.

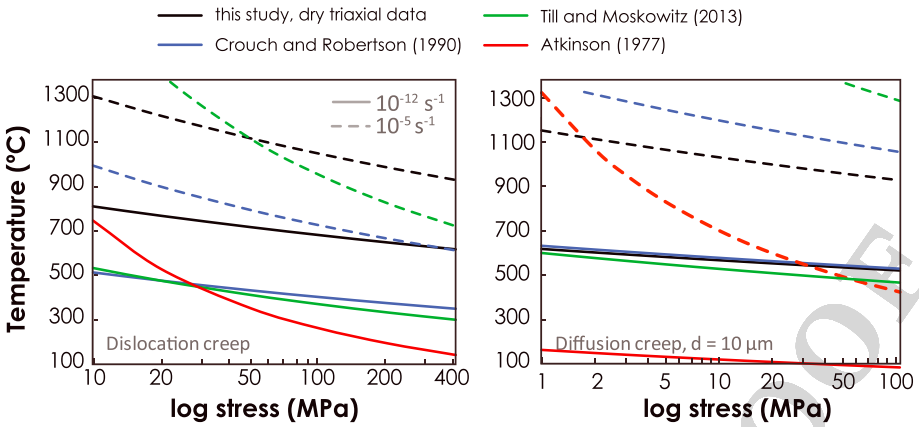

Figure 9. Best-fit flow law for creep of dry magnetite determined in this study compared with previously reported magnetite flow laws.

4. Discussion

4.1. Comparison With Previous Work

No systematic experimental studies have previously characterized the deformation behavior of magnetite for applications to geologic settings. Deformation mechanism maps for magnetite were first constructed by Atkinson (1977) based on theoretical predictions and low-temperature ($T < 550$ °C) diffusion data of Castle and Surman (1967), with flow law parameters of $\log A = -11.7$ MPa^{-n} s^{-1}, $n = 3$, and $Q = 65.2$ kJ/mol for the dislocation creep regime. Crouch and Robertson (1990) produced deformation mechanism maps based on magnetite creep tests performed in a four-point bending apparatus, with reported dislocation creep parameters of $n = 3.1$, $\log A = 3.4$ MPa^{-n} s^{-1}, and $Q = 280$ kJ/mol and poorly constrained diffusion creep parameters of $n = 1.0$, $\log A = 3.4$ MPa^{-n} s^{-1}, and $Q = 264$, the latter of which was interpreted in terms of Nabarro-Herring creep. Till and Moskowitz (2013) proposed a revised set of theoretical creep equations based on high temperature ($T = 500$–800 °C) data for oxygen diffusion in magnetite from Giletti and Hess (1988), yielding flow law parameters of $\log A = -4.6$ MPa^{-n} s^{-1}, $n = 3$, and $Q = 182$ kJ/mol for dislocation creep and $\log A = 0.27$ MPa^{-n} s^{-1}, $n = 1$, $m = -3$, and $Q = 124$ kJ/mol for Coble creep.

All previously proposed flow laws are compared in Figure 9 with the best-fit rate laws from our dry triaxial experiments. Data are shown for strain rates of 10^{-12} and 10^{-5} s^{-1} chosen to represent geologic and laboratory creep rates, respectively. For a given strain rate, the Crouch and Robertson (1990) flow laws predict dislocation creep at much lower temperatures or stresses than those measured in our experiments. Their lower flow stresses probably result from their different experimental setup using a bending apparatus, which may promote brittle processes such as microcracking to a greater extent than our compression experiments. The dislocation creep law of Till and Moskowitz (2013) is similar to that of Crouch and Robertson (1990) at the lower strain rate and intermediate between our dry triaxial rates and Crouch and Robertson (1990) at stresses above 50 MPa. The Atkinson (1977) flow laws predict very low dislocation creep temperatures at geologic strain rates and no deformation at laboratory strain rates. Our diffusion creep laws normalized to 10-μm grain size (Figure 9b) are very close to those of both Till and Moskowitz (2013) and Crouch and Robertson (1990) at geological strain rates but indicate weaker magnetite behavior than either of the latter studies at laboratory strain rates. Atkinson (1977) predicts unrealistically low deformation temperatures and stresses at both strain rates. As outlined in the following section, we interpret the huge difference between predicted stresses from the various flow laws to be caused by different water content, where our data represent nominally dry conditions. In addition, a direct comparison between theoretical and different experimental approaches is probably problematic regarding the underlying assumptions and uncertainties.

4.2. Activation Energy of Magnetite Creep

We determined an activation energy for dislocation creep of nominally dry magnetite of 463 ± 19 kJ/mol. This value is close to the creep activation energy of 434 kJ/mol determined for $NiFe_2O_4$ single crystals by Rabier et al. (1976) and the value of 416 ± 16 kJ/mol reported by Lawlis et al. (2001) for dislocation creep of spinel-structured Ni_2GeO_4 aggregates. For dry diffusion creep, we obtained $Q = 314 \pm 15$ kJ/mol, which indicates a significant proportion of grain boundary diffusion creep assuming that the temperature

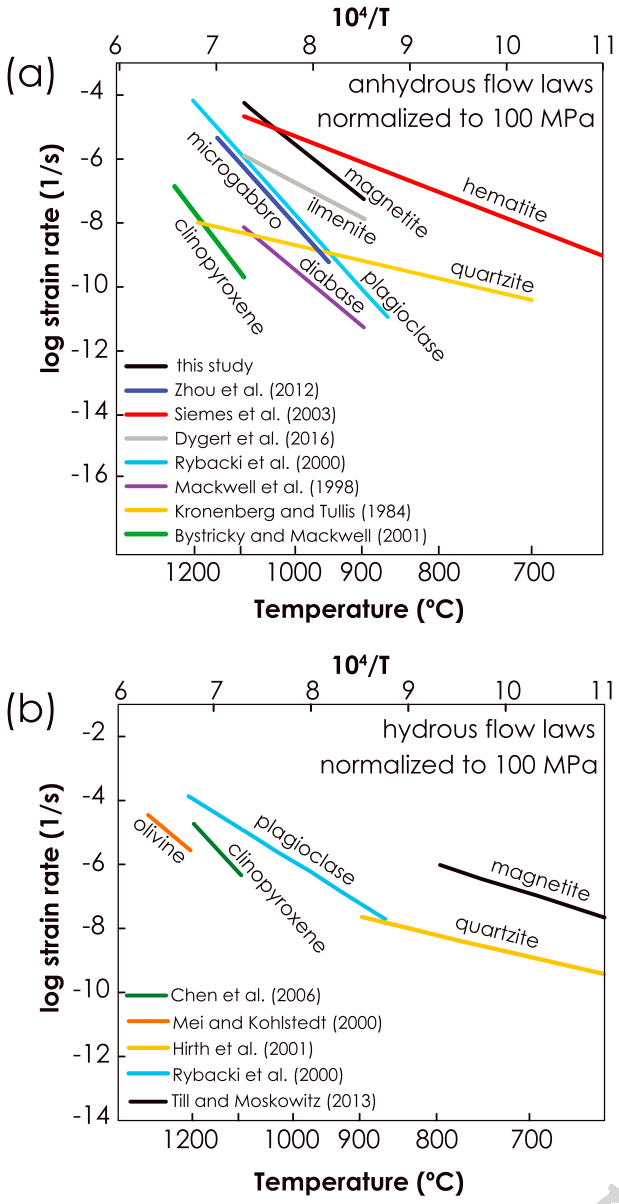

Figure 10. (a) Best-fit flow law for dislocation creep of dry magnetite determined in this study compared with dislocation creep data for dry silicate minerals and oxides from other studies. (b) Experimental dislocation creep data for silicate minerals under hydrous conditions with proposed magnetite flow law of Till and Moskowitz (2013). All data are normalized to a differential stress of 100 MPa.

sensitivity of dislocation creep is governed by self-diffusion of the slowest species along the fastest path (Weertman, 1968). This conclusion is consistent with the measured grain size exponent of $m = -2.4 \pm 0.5$. Note that the activation energy for diffusion creep coincides with that for grain growth (271 ± 41 kJ/mol) within error bars.

The determined activation energies for both dislocation and diffusion creep of dry magnetite in our experiments are significantly larger than the published activation energies for oxygen self-diffusion in wet magnetite, which is much slower than iron diffusion (Dieckmann & Schmalzried, 1977) and should therefore be rate limiting. An O self-diffusion activation energy of 71 kJ/mol was reported at T = 250–550 °C for oxygen exchange between magnetite and water vapor in an early study by Castle and Surman (1967), and Giletti and Hess (1988) determined an activation energy of 188 kJ/mol for oxygen diffusivity in magnetite under hydrothermal conditions at T = 500–800 °C. Reported values for O self-diffusion in dry Mg-Al spinel vary from 404 to 439 kJ/mol (Ando & Oishi, 1974; Ryerson & McKeegan, 1994). These quite different reported activation energies demonstrate that the influence of water on diffusivity in oxides is substantial.

The presence of water has consistently been shown to elevate diffusivity (Costa & Chakraborty, 2008) and therefore deformation rates, as well as lower the activation energy for oxygen self-diffusion in several minerals (Farver, 2010). No data are available for O self-diffusion in dry magnetite, but it is unsurprising that the dry triaxial creep experiments yield significantly higher activation energies than those reported for diffusion in wet magnetite. However, the activation energy of 421 kJ/mol determined for diffusion creep of the water-bearing sample MP10, while only based on three temperatures, is much higher than the value of 314 kJ/mol for diffusion creep in the dry magnetite samples. The grain size sensitivity for wet magnetite creep is unknown, and the mean grain size exponent of −2.4 observed in our dry diffusion creep data does not allow us to discriminate between Nabarro-Herring creep and Coble creep. It is possible that the larger grain size and relatively low creep stresses in sample MP10 promoted more Nabarro-Herring creep than in the dry experiments, which might be expected to have higher activation energies than deformation dominated by Coble creep even in dry conditions.

4.3. Geological Implications

Figure 10a presents our experimental flow law for dry magnetite dislocation creep alongside those of various silicate rocks and minerals deformed under dry conditions. This comparison indicates that magnetite will be weaker than most silicate phases in dry igneous rocks such as oceanic gabbros over a broad range of crustal deformation temperatures. The data for vacuum-dried quartzite from Kronenberg and Tullis (1984) indicate that magnetite should be weaker than quartz at high temperatures, but it will become relatively stronger with decreasing temperature. Although few studies have experimentally determined creep laws for gabbros, the strength of gabbroic rocks may be estimated by comparing data for partially molten dry microgabbro (Zhou et al., 2012), dry diabase (Mackwell et al., 1998), pyroxene (Bystricky & Mackwell, 2001), and plagioclase (Rybacki & Dresen, 2000) in Figure 10a. Data for other common Fe-oxide minerals such as hematite (Siemes et al., 2003) and ilmenite (Dygert et al., 2016) indicate that they are similarly likely to be weaker than many silicate phases. One implication of this finding is that rocks containing high concentrations of Fe-Ti-oxide minerals may undergo ductile deformation at lower temperatures than oxide-poor rocks, and strain may preferentially be localized in oxide-rich layers or regions, as has been theorized for oxide-rich shear zones in oceanic core complexes (Cannat, 1991) and banded iron formations (Zheng et al., 2017). Where mixtures

of Fe-bearing oxide phases are present, less strain partitioning is expected between magnetite and ilmenite or hematite based on their relatively similar strengths at high temperatures.

Magnetite is the most prominent ferromagnetic phase in the Earth's crust and exerts a major control on the magnetic properties of rocks. Magnetic anisotropy measurements are an increasingly common method for characterizing mineral textures in deformed rocks, and the presence of magnetite strongly influences the character of the magnetic anisotropy (Borradaile & Jackson, 2004). The relative weakness of magnetite shown in Figure 10 indicates that in crystalline silicate rocks containing small amounts of magnetite, isolated magnetite grains are expected to undergo the same strain as the silicate matrix. In this case, the shape anisotropy and alignment of deformed magnetite grains will reflect the bulk strain of the silicate matrix, according to the passive model of Owens (1974) and Hrouda (1993).

A clear water-weakening effect was observed in our hydrous triaxial deformation experiment compared to dry aggregates. However, quantitative determinations of magnetite creep dependence on water fugacity require further experiments. Because the Till and Moskowitz (2013) flow laws are based on water-present oxygen diffusivities from Giletti and Hess (1988), their flow laws may be taken as a first approximation of magnetite creep rates under hydrous conditions. Their dislocation creep flow law is plotted in Figure 10b in comparison with dislocation creep data for plagioclase (Rybacki & Dresen, 2000), olivine (Mei & Kohlstedt, 2000), clinopyroxene (Chen et al., 2006), and quartzite (Hirth et al., 2001) under hydrous conditions. Magnetite is again expected to be weaker than the major silicate phases at a broad range of temperatures. This prediction is supported by recent experimental (Gonçalves et al., 2015) and field investigations (Zheng et al., 2017) of banded iron formations in which magnetite has been observed to behave as a weak ductile phase during deformation of the relatively competent quartz layers or matrix.

It is crucial to note that the rates of both creep and oxygen diffusion in magnetite have been shown to depend strongly on oxygen fugacity (Domınguez-Rodrıguez et al., 2002; Millot & Niu, 1997). The nature of this dependence changes in sign across the range of the magnetite stability field and a difference of two log units in oxygen fugacity can cause magnetite strain rates to vary by an order of magnitude. In rocks for which the oxygen fugacity is not well known, this influence may lead to large uncertainties on the actual strength of magnetite in natural settings. The effect of composition, such as Ti content, on the strength of magnetite is yet to be investigated.

5. Conclusions

This study presents a detailed characterization of creep behavior in synthetic magnetite aggregates as a function of temperature and stress. A multivariate linear regression analysis was performed to determine the best-fit flow laws from the experimental data. Grain-size dependence and water weakening effects were additionally observed; however, more precise characterizations of the grain size exponent and water fugacity dependence require further experimental quantification. Microstructures in the deformed samples indicate that incipient subgrain formation occurred along with dislocation creep but was not accompanied by development of CPO at low strain. The observed activation energy of dry magnetite creep agrees poorly with that for oxygen diffusion in wet magnetite, likely affected by the presence of hydrous species. Based on the experimental flow laws determined here, magnetite is expected to behave as a weak phase relative to many rock-forming silicate minerals over a broad range of deformation temperatures. However, whether magnetite and related Fe-oxides behave as relatively strong or weak phases in natural silicate rocks will depend strongly on water content, oxygen fugacity, and mineral compositions.

Acknowledgments
The Alexander von Humboldt Foundation is thanked for supporting J. Till with a research stay in Germany. We are grateful to Dieter Rhede for assistance with electron microprobe analysis and to Richard Wirth and Anja Schreiber for assistance with TEM imaging and FIB sample preparation. The authors thank Ian Jackson and the associate editor for constructive review comments. All processed experimental data used in this study are contained in the tables and figures for this paper. Experimental results from other studies can be found in the references cited.

References

Agar, S., & Lloyd, G. (1997). Deformation of Fe-Ti oxides in gabbroic shear zones from the Mark area. In J. Karson, M. Cannat, D. Miller, & D. Elthon (Eds.), *Proceedings of the Ocean Drilling Program: Scientific Results* (Vol. 153, pp. 123–141). Texas: Ocean Drilling Program.

Ando, K., & Oishi, Y. (1974). Self-diffusion coefficients of oxygen ion in single crystals of MgO*n*Al_2O_3spinels. *The Journal of Chemical Physics*, *61*, 625.

Atkinson, B. (1977). The kinetics of ore deformation: Its illustration and analysis by means of deformation-mechanism maps. *Geologiska Föreningens i Stockholm Förhandlingar*, *2*(569), 186–197.

Atkinson, H. (1988). Overview no. 65: Theories of normal grain growth in pure single phase systems. *Acta Metallurgica*, *36*(3), 469–491.

Blackman, D., Ildefonse, B., John, B., Ohara, Y., Miller, D., & MacLeod, C. (2006). Proceedings of the Integrated Ocean Drilling Program. In *Integrated Ocean Drilling Program Management International, Inc*, *304/305*, College Station, TX.

Borradaile, G. J., & Jackson, M. (2004). Anisotropy of magnetic susceptibility (AMS): Magnetic petrofabrics of deformed rocks. *Geological Society, London, Special Publications*, *238*(1), 299–360.
Brook, R. (1976). Controlled grain growth, *Treatise on Materials Science & Technology* (Vol. 9, pp. 331–364): Elsevier.
Bunge, H. (1982). *Texture Analysis in Materials Science*. London: Butterworths.
Bystricky, M., & Mackwell, S. (2001). Creep of dry clinopyroxene aggregates. *Journal of Geophysical Research*, *106*(B7), 13443–13454. https://doi.org/10.1029/2001JB000333
Cannat, M. (1991). Plastic deformation at an oceanic spreading ridge: A microstructural study of the Site 735 gabbros (southwest Indian Ocean). In e. a. RP Von Herzen PT Robinson (Ed.), *Proceedings of the Ocean Drilling Program: Scientifics Results* (Vol. 118, pp. 399–408). College Station, TX: Ocean Drilling Program.
Castle, J., & Surman, P. (1967). Self-diffusion of oxygen in magnetite: Techniques for sampling and isootopic analysis of micro quantities of water. *Journal of Physical Chemistry*, *71*(13), 4255–4259.
Chen, S., Hiraga, T., & Kohlstedt, D. (2006). Water weakening of clinopyroxene in the dislocation creep regime. *Journal of Geophysical Research*, *111*, B08203. https://doi.org/10.1029/2005JB003885
Costa, F., & Chakraborty, S. (2008). The effect of water on Si and O diffusion rates in olivine and implications for transport properties and processes in the upper mantle. *Physics of the Earth and Planetary Interiors*, *166*(1–2), 11–29.
Covey-Crump, S. J. (1997). The normal grain growth behaviour of nominally pure calcitic aggregates. *Contributions to Mineralogy and Petrology*, *129*(2), 239–254.
Crouch, A., & Robertson, J. (1990). Creep and oxygen diffusion in magnetite. *Acta Metallurgica et Materialia*, *38*(12), 2567–2572. https://doi.org/10.1016/0956-7151(90)90268-L
Dieckmann, R., & Schmalzried, H. (1977). Defects and cation diffusion in magnetite (I). *Berichte der Bunsengesellschaft für Physikalische Chemie*, *81*(3), 344–347.
Dimanov, A., & Jaoul, O. (1998). Calcium self-diffusion in diopside at high temperature: Implications for transport properties. *Physics and Chemistry of Minerals*, *26*(2), 116–127.
Domınguez-Rodrıguez, D., Castaing, J., & Millot, F. (2002). The influence of oxygen partial pressure on recovery creep in magnetite single crystals. *Journal of Physics and Chemistry of Solids*, *63*(2), 185–191.
Dupas-Bruzek, C., Tingle, T. N., Green II, H. W., Doukhan, N., & Doukhan, J. C. (1998). The rheology of olivine and spinel magnesium germanate (Mg2GeO4): TEM study of the defect microstructures. *Physics and Chemistry of Minerals*, *25*(7), 501–514.
Dygert, N., Hirth, G., & Liang, Y. (2016). A flow law for ilmenite in dislocation creep: Implications for lunar cumulate mantle overturn. *Geophysical Research Letters*, *43*, 532–540. https://doi.org/10.1002/2015GL066546
Farver, J. R. (2010). Oxygen and hydrogen diffusion in minerals. *Reviews in Mineralogy and Geochemistry*, *72*(1), 447–507.
Faul, U. H., Cline II, C. J., Berry, A., Jackson, I., & Garapić, G. (2018). Constraints on oxygen fugacity within metal capsules. *Physics and Chemistry of Minerals*, *45*(6), 497–509.
Freund, D., Rybacki, E., & Dresen, G. (2001). Effect of impurities on grain growth in synthetic calcite aggregates. *Physics and Chemistry of Minerals*, *28*(10), 737–745.
Freund, D., Wang, Z., Rybacki, E., & Dresen, G. (2004). High-temperature creep of synthetic calcite aggregates: Influence of Mn-content. *Earth and Planetary Science Letters*, *226*(3), 433–448.
Frost, H., & Ashby, M. (1982). *Deformation Mechanism Maps: The Plasticity and Creep of Metals and Ceramics*. Oxford; New York: Pergamon Press.
Giletti, B., & Hess, K. (1988). Oxygen diffusion in magnetite. *Earth and Planetary Science Letters*, *89*(1), 115–122.
Gonçalves, C. C., Gonçalves, L., & Hirth, G. (2015). The effects of quartz recrystallization and reaction on weak phase interconnection, strain localization and evolution of microstructure. *Journal of Structural Geology*, *71*, 24–40.
Hansen, L., Zimmerman, M., & Kohlstedt, D. L. (2011). Grain boundary sliding in San Carlos olivine: Flow law parameters and crystallographic-preferred orientation. *Journal of Geophysical Research*, *116*, B08201. https://doi.org/10.1029/2011JB008220
Hennig-Michaeli, C., & Siemes, H. (1975). Zwillungsgleitung beim Magnetite. *Neues Jahrbuch für Mineralogie - Abhandlungen*, *123*, 330–334.
Hennig-Michaeli, C., & Siemes, H. (1982). Compression experiments on natural magnetite crystals at 200° C and 400° C at 400 MPa confining pressure, *Issues in rock mechanics: Proceedings, Twenty-Third Symposium on Rock Mechanics, the University of California, Berkeley, California, August 25-27* (pp. 380). Berkeley, California: American Rock Mechanics Association.
Hirth, G., Teyssier, C., & Dunlap, J. W. (2001). An evaluation of quartzite flow laws based on comparisons between experimentally and naturally deformed rocks. *International Journal of Earth Sciences*, *90*(1), 77–87.
Hornstra, J. (1960). Dislocations, stacking faults and twins in the spinel structure. *Journal of Physics and Chemistry of Solids*, *15*(3–4), 311–323.
Hrouda, F. (1993). Theoretical models of magnetic anisotropy to strain relationship revisited. *Physics of the Earth and Planetary Interiors*, *77*(3–4), 237–249.
Karato, S. (1989). Grain growth kinetics in olivine aggregates. *Tectonophysics*, *168*(4), 255–273.
Karson, J., Cannat, M., Miller, D., & Elthon, D. (Eds.) (1997). *Proceedings of the Ocean Drilling Program: Scientific Results Edited by* Karson, J., Cannat, M., Miller, D., & Elthon, D., (Vol. 153). College Station, TX: Ocean Drilling Program.
Kronenberg, A. K., & Tullis, J. (1984). Flow strengths of quartz aggregates: Grain size and pressure effects due to hydrolytic weakening. *Journal of Geophysical Research*, *89*(B6), 4281–4297. https://doi.org/10.1029/JB089iB06p04281
Lawlis, J., Zhao, Y., & Karato, S. (2001). High-temperature creep in a Ni_2GeO_4: A contribution to creep systematics in spinel. *Physics and Chemistry of Minerals*, *28*(8), 557–571.
Mackwell, S., Zimmerman, M., & Kohlstedt, D. (1998). High-temperature deformation of dry diabase with application to tectonics on Venus. *Journal of Geophysical Research*, *103*(B1), 975–984. https://doi.org/10.1029/97JB02671
Mei, S., & Kohlstedt, D. (2000). Influence of water on plastic deformation of olivine aggregates: 2. Dislocation creep regime. *Journal of Geophysical Research*, *105*(B9), 21471–21481. https://doi.org/10.1029/2000JB900180
Millot, F., & Niu, Y. (1997). Diffusion of O^{18} in Fe_3O_4: An experimental approach to study the behavior of minority defects in oxides. *Journal of Physics and Chemistry of Solids*, *58*(1), 63–72. https://doi.org/10.1016/S0022-3697(96)00101-1
Muller, P., & Siemes, H. (1972). Zur Festigkeit und Gefugeregulung von experimentell verformten Magnetiterzen. *Neues Jahrbuch für Mineralogie - Abhandlungen*, *117*, 39–60.
Nabarro, F. (1967). Steady-state diffusional creep. *Philosophical Magazine*, *16*(140), 231–237.
Natland, J. (2002). Magnetic susceptibility as an index of the lithology and composition of gabbros, ODP Leg 176, Hole 735B, Southwest Indian Ridge. In *Proceedings of the Ocean Drilling Program: Scientific Results*, *176*, College Station, TX, pp. 1–69.

Owens, W. (1974). Mathematical model studies on factors affecting the magnetic anisotropy of deformed rocks. *Tectonophysics*, *24*(1–2), 115–131.

Paterson, M. S. (1990). Rock deformation experimentation. In A. G. Duba, W. B. Durham, J. W. Handin, & H. F. Wang (Eds.), *The Brittle-Ductile Transition in Rocks* (Vol. 56, pp. 187–194). Washington, DC: American Geophysical Union.

Prunier, A. R., & Hewitt, D. A. (1981). Calculation of temperature-oxygen fugacity tables for H_2-CO_2 gas mixtures at one atmosphere total pressure. *Geological Society of America Bulletin*, *92*(7 Part II), 1039–1068.

Rabier, J., Veyssière, P., & Grilhé, J. (1976). Plastic deformation of $Ni_{0.66}Fe_{2.34}O_4$ spinel ferrite single crystals. *Journal of Material Science*, *11*(1), 193–195.

Rybacki, E., & Dresen, G. (2000). Dislocation and diffusion creep of synthetic anorthite aggregates. *Journal of Geophysical Research*, *105*(B11), 26017–26036. https://doi.org/10.1029/2000JB900223

Rybacki, E., Gottschalk, M., Wirth, R., & Dresen, G. (2006). Influence of water fugacity and activation volume on the flow properties of fine-grained anorthite aggregates. *Journal of Geophysical Research*, *111*, B03203. https://doi.org/10.1029/2005JB003663

Ryerson, F., & McKeegan, K. D. (1994). Determination of oxygen self-diffusion in åkermanite, anorthite, diopside, and spinel: Implications for oxygen isotopic anomalies and the thermal histories of Ca-Al-rich inclusions. *Geochimica et Cosmochimica Acta*, *58*(17), 3713–3734.

Siemes, H., Klingenberg, B., Rybacki, E., Naumann, M., Schäfer, W., Jansen, E., & Kunze, K. (2008). Glide systems of hematite single crystals in deformation experiments. *Ore Geology Reviews*, *33*(3), 255–279.

Siemes, H., Klingenberg, B., Rybacki, E., Naumann, M., Schäfer, W., Jansen, E., & Rosière, C. (2003). Texture, microstructure, and strength of hematite ores experimentally deformed in the temperature range 600–1100° C and at strain rates between 10^{-4} and $10^{-6}s^{-1}$. *Journal of Structural Geology*, *25*(9), 1371–1391.

Siemes, H., Rybacki, E., Klingenberg, B., & Rosière, C. (2011). Development of a recrystallized grain size piezometer for hematite based on high-temperature torsion experiments. *European Journal of Mineralogy*, *23*(3), 293–302.

Till, J., Guyodo, Y., Lagroix, F., Ona-Nguema, G., & Brest, J. (2014). Magnetic comparison of abiogenic and biogenic alteration products of lepidocrocite. *Earth and Planetary Science Letters*, *395*, 149–158.

Till, J., & Moskowitz, B. (2013). Magnetite deformation mechanism maps for better prediction of strain partitioning. *Geophysical Research Letters*, *40*, 697–702. https://doi.org/10.1002/grl.50170

Till, J., & Moskowitz, B. (2014). Deformation microstructures and magnetite texture development in synthetic shear zones. *Tectonophysics*, *629*, 211–223.

Till, J., Moskowitz, B., & Jackson, M. (2012). High-temperature magnetic fabric development from plastically deformed magnetite in experimental shear zones. *Geophysical Journal International*, *189*(1), 229–239.

Vaughan, P., & Kohlstedt, D. (1981). Cation stacking faults in magnesium germanate spinel. *Physics and Chemistry of Minerals*, *7*(6), 241–245.

Veyssiére, P., & Carter, C. (1988). Dissociation of dislocations in $MgAl_2O_4$ spinel deformed at low temperatures. *Philosophical Magazine Letters*, *57*(4), 211–220.

Weertman, J. (1968). Dislocation climb theory of steady-state creep. *Transactions of the American Society of Metals*, *61*, 681–694.

Zheng, Y., Han, X., Gao, X., Geng, X., Chen, X., & Liu, J. (2017). Enrichment of iron ores by folding in the BIF-hosted deposit: A case study from the Archean Qian'an iron deposit, North China Craton. *Geological Journal*.

Zhou, Y., Rybacki, E., Wirth, R., He, C., & Dresen, G. (2012). Creep of partially molten fine-grained gabbro under dry conditions, *117*, B05204. https://doi.org/10.1029/2011JB008646

Q8